EUROPEAN JOURNAL OF COMPUTATIONAL MECHANICS, 2017
VOL. 26, NOS. 5–6, 443–472
https://doi.org/10.1080/17797179.2017.1354575

Taylor & Francis
Taylor & Francis Group

OPEN ACCESS Check for updates

On contact modelling in isogeometric analysis

R. P. R. Cardoso and O. B. Adetoro

Department of Mechanical, Aerospace and Civil Engineering, Brunel University London, London, UK

ABSTRACT

IsoGeometric Analysis (IGA) has proved to be a reliable numerical tool for the simulation of structural behaviour and fluid mechanics. The main reasons for this popularity are essentially due to: (i) the possibility of using higher order polynomials for the basis functions; (ii) the high convergence rates possible to achieve; (iii) the possibility to operate directly on CAD geometry without the need to resort to a mesh of elements. The major drawback of IGA is the non-interpolatory characteristic of the basis functions, which adds a difficulty in handling essential boundary conditions and makes it particularly challenging for contact analysis. In this work, the IGA is expanded to include frictionless contact procedures for sheet metal forming analyses. Non-Uniform Rational B-Splines (NURBS) are going to be used for the modelling of rigid tools as well as for the modelling of the deformable blank sheet. The contact methods developed are based on a two-step contact search scheme, where during the first step a global search algorithm is used for the allocation of contact knots into potential contact faces and a second (local) contact search scheme where point inversion techniques are used for the calculation of the contact penetration gap. For completeness, elastoplastic procedures are also included for a proper description of the entire IGA of sheet metal forming processes.

ARTICLE HISTORY
Received 12 January 2017
Accepted 10 July 2017

KEYWORDS
Isogeometric analysis; NURBS; contact analysis; sheet metal forming

1. Introduction

The constant drive for more efficient and accurate numerical simulations creates the need for more effective and accurate computational methods. Examples of such methods are meshless methods and, more recently, Isogeometric Analysis (IGA) based on Non-Uniform Rational B-Splines (NURBS). IGA is a powerful numerical tool for structural and fluid analyses because it allows the numerical simulations to be conducted directly on the geometric model without the necessity of resorting to a mesh of elements for the interpolation of the field variables.

CONTACT R. P. R. Cardoso Rui.Cardoso@brunel.ac.uk

© 2017 The Author(s). Published by Informa UK Limited, trading as Taylor & Francis Group.
This is an Open Access article distributed under the terms of the Creative Commons Attribution-NonCommercial-NoDerivatives License (http://creativecommons.org/licenses/by-nc-nd/4.0/), which permits non-commercial re-use, distribution, and reproduction in any medium, provided the original work is properly cited, and is not altered, transformed, or built upon in any way.

IGA was introduced successfully in the work of Hughes, Cottrel, and Bazilevs (2005). The isogeometric concept means that the same approximation basis functions are used for the representation of the geometry and for the approximation of the field variables. The main differences between IGA and the Finite Element Method (FEM) are as follows: (i) the basis functions in IGA are always positive; (ii) a higher degree for the polynomial of the basis functions can be used; (iii) the basis functions can be C^{p-1} continuous, where p is the degree of the polynomial used; (iv) smoother contact analysis. There is however some difficulties in handling essential boundary conditions and local constraints for contact because the basis functions are not interpolatory. Some important works on isogeometric analysis were already published and we can distinguish the work by Cottrell, Hughes, and Reali (2007) on the refinement and continuity in isogeometric structural analysis, the work by Cottrell, Reali, Bazilevs, and Hughes (2006) and Hughes, Reali, and Sangalli (2008) on the isogeometric analysis for structural dynamics and vibrations, the work by Hughes, Reali, and Sangalli (2010) on the study of numerical quadrature rules for a NURBS-based isogeometric analysis, the work by Benson, Bazilevs, Hsu, and Hughes (2010) who extended the isogeometric analysis to the Reissner–Mindlin shell type formulations and Echter and the work by Echter and Bischoff (2010) who studied the numerical efficiency of NURBS together with the Discrete Shear Gap formulation to overcome the transverse shear locking. Taylor (2010) performed a study on the modelling of nearly incompressible materials under the IGA context. Recently, Cardoso and Cesar de Sa (2012) applied the Enhanced Assumed Strain (EAS) formulation, very typical from the finite element method, into the subspace analysis of incompressible deformations, such as the ones present in elastoplastic simulations, and within the IGA framework. In the work, the subspace of incompressible deformation of a 3D IsoGeometric 'element' was firstly analysed for different degrees of the polynomial basis functions and, thereafter, additional enhancing variables were introduced to enlarge that subspace of incompressible deformations. The enhancing variables could be eliminated at an IGA 'element' level and it was then verified that the subspace of incompressible deformations was effectively augmented providing additional deformation flexibility to the IsoGeometric formulation. Later, Cardoso and Cesar de Sa (2014) developed a new numerical technique to alleviate different kind of locking pathologies in IGA. The projection scheme developed in Cardoso and Cesar de Sa (2014) was based on the Moving Least Square (MLS) technique which allowed the projection procedure to be general and easily adapted to any degree of the NURBS basis functions. Using this procedure, the reduced strain–displacement matrices were extrapolated or projected into the full quadrature space by means of a moving least square minimisation of the assumed strain field. The method was then applied to alleviate the volumetric locking (equivalent to the B-bar approach Cesar de Sa & Natal Jorge, 1999; Cesar de Sa & Owen, 1986; Hughes, 2000;

Hughes, Cohen, & Haroun, 1978) as well as onto alleviate the transverse shear locking for thin-walled structures (shell or solid-shell formulations).

The basic steps/procedures for the numerical treatment of elastoplasticity in the context of sheet metal forming processes are also presented in this work. The numerical simulation of elastoplasticity under the IGA framework follows exactly the same procedures as the simulation of elastoplasticity in the context of the classical finite element method. The decision to include a section on this subject in this paper is simply for the completeness of the paper rather than a notion of providing any new contribution on this area. For the interested reader on the numerical simulation of elastoplastic effects, the works by Yoon, Yang, and Chung (1999), Cardoso and Yoon (2005) and Ortiz and Simo (1986) are recommended.

The numerical simulation of contact procedures is already well established for the finite element method, where the reference works by Laursen and Simo (1993), Laursen (2002) and Wriggers (2002) are all representative of the state-of-the-art in this area. The developments for contact analysis in IGA are still very few and so it can be said that this represents the innovative contribution of this paper. We developed a global and local contact search procedures for IGA as well as the weak formulation to include contact as local constraints under the IGA framework. The rigid tools are modelled as rigid NURBS surfaces and the deformable blank sheet is also modelled by using an IsoGeometric approximation from the use of NURBS basis functions. Therefore, the main objective of this work is to demonstrate the benefits and challenges of contact modelling in the context of IsoGeometric analysis.

2. Non-Uniform Rational B-Splines (NURBS)

B-Splines, rational B-Splines and Non-Uniform Rational B-Splines (NURBS) have been extensively used by the computer-aided design community for geometric modelling of structures and parts. Detailed overview of B-Spline curves, B-Splines surfaces and NURBS can be found in Piegl and Tiller (1996) and Cottrell, Hughes, and Bazilevs (2009). Some properties, definitions and features on NURBS are very briefly reviewed in this section.

2.1. Knot vectors

In this work only open knot vectors are going to be used. An open knot vector is a set of non-negative parametric coordinates which are repeated $p+1$ times at the beginning and at the end of the vector (p is the degree of the polynomial basis functions). For one-dimensional basis functions of degree p, the following generic open knot vector can be defined:

$$\Xi = \left\{ \xi_1, \ldots, \xi_{p+1}, \ldots, \xi_{m+1}, \ldots, \xi_{m+p+1}, \right\} \tag{1}$$

where m is the number of control points or basis functions. The basis functions of degree p have $p-1$ continuous derivatives. More than one knot can be considered at the same parametric coordinate and it is thus referred as a repeated knot. An important property of repeated knots is that the continuous derivative of their basis functions is decreased by the number of times the knot is repeated. Also, the basis functions are interpolatory only if the knot's multiplicity is the same as the polynomial's degree p (Piegl & Tiller, 1996).

2.2. Control points and basis functions

For a specific local parametric coordinate ξ from an open knot vector and for a degree p of the polynomial, the basis functions are obtained recursively from the following recursive formulae (Cottrell et al., 2009; Hughes et al., 2005; Piegl & Tiller, 1996):

$$N_I^p = \frac{\xi - \xi_I}{\xi_{I+p} - \xi_I} N_I^{p-1}(\xi) + \frac{\xi_{I+p+1} - \xi}{\xi_{I+p+1} - \xi_I} N_{I+1}^{p-1}(\xi), \tag{2}$$

where I is the index for the basis functions. The formula for the basis functions at Equation (2) must be initialised from piecewise basis functions corresponding to the polynomial order $p = 0$, i.e.:

$$N_I^0(\xi) = \begin{cases} 1 & \text{if} \quad \xi_I \leq \xi < \xi_{I+1} \\ 0 & \text{otherwise} \end{cases} \tag{3}$$

Hughes et al. (2005) and Bazilevs et al. (2010) addressed the most fundamental properties of the basis functions, which make them suitable for isogeometric analysis:

(1) They form a partition of unity, i.e.:

$$\sum_{J=1}^{m} N_J^p(\xi) = 1, \quad \xi \in \Xi = [\xi_1, \xi_{m+p+1}]; \tag{4}$$

(2) The support of each $N_J^p(\xi)$ is compact and contained in $[\xi_J, \xi_{J+p+1}]$;
(3) The basis functions are non-negative, that is, $\forall \xi \rightarrow N_J^p(\xi) \geq 0$;
(4) Control of continuity with repeated knots. This property allows for smooth basis functions for higher degree polynomials but it also allows controlling the interpolatory characteristic of the basis functions by adjusting the multiplicity of the repeated knots to be equal to the degree p of the polynomial.

A B-spline surface can be constructed from a net of control points A_{IJ} and from a two-dimensional knot set $\Xi \times H$, with $H = \{\eta_1, \eta_2, \ldots, \eta_{n+q+1}\}$ and q and n being the degree and the number of control points or basis functions along the η direction, respectively. A B-spline surface is thus obtained from the

following linear combination:

$$S^{p,q}(\xi,\eta) = \sum_{I=1}^{n}\sum_{J=1}^{m} N_I^q(\eta)\, N_J^p(\xi)\, A_{IJ}. \tag{5}$$

For a solid B-Spline constructed from a net of control points A_{IJK} and from a three-dimensional set $\Xi \times H \times Z$, with $Z = \{\zeta_1, \zeta_2, \ldots, \zeta_{l+r+1}\}$ and r and l being the degree and the number of control points or basis functions along the ζ direction, respectively, the following linear combination can be defined for local approximations:

$$T^{p,q,r}(\xi,\eta,\zeta) = \sum_{k,I,J=1}^{l,n,m} N_K^r(\zeta)\, N_I^q(\eta)\, N_J^p(\xi)\, A_{IJK}. \tag{6}$$

The Non-Uniform Rational B-Splines (NURBS) are rational polynomials obtained from a weighted linear combination of the basis functions with their control points as coefficients. In this way, a NURBS surface can be constructed from a two-dimensional knot set $\Xi \times H$ and from a net of control points A_{IJ} and weights W_{IJ} as follows:

$${}^{w}S^{p,q}(\xi,\eta) = \frac{\sum_{I=1}^{n}\sum_{J=1}^{m} N_I^q(\eta)\, N_J^p(\xi)\, W_{IJ} A_{IJ}}{W} \tag{7}$$

while the NURBS solid is constructed from a three-dimensional knot set $\Xi \times H \times Z$ and a net of control points A_{IJK} and weights W_{IJK}:

$${}^{w}T^{p,q,r}(\xi,\eta,\zeta) = \frac{\sum_{k,I,J=1}^{l,n,m} N_K^r(\zeta)\, N_I^q(\eta)\, N_J^p(\xi)\, W_{IJK} A_{IJK}}{W}. \tag{8}$$

with

$$W = \sum_{I=1}^{n}\sum_{J=1}^{m} N_I^q(\eta)\, N_J^p(\xi)\, W_{IJ} \tag{9}$$

for the NURBS surface and:

$$W = \sum_{k=1}^{l}\sum_{I=1}^{n}\sum_{J=1}^{m} N_K^r(\zeta)\, N_I^q(\eta)\, N_J^p(\xi)\, W_{IJK} \tag{10}$$

for a NURBS solid.

3. IsoGeometric Analysis of 3D solid structures

In this section the kinematics is detailed together with the derivation of the incremental equations of motion for IGA. The formulation is based on the 3D

continuum description for the thin-walled blank sheet, which includes translational degrees of freedom only at the control points. In this section, the local constraints for IGA are also included into the equations for the virtual work.

3.1. Kinematics

The physical spatial region of a IsoGeometric (IG) 'element' is mapped from the parametric knot coordinates (ξ, η, ζ) and is defined between two consecutive knots along ξ, η and ζ parametric directions. By considering one IG 'element', the coordinates of a point can be obtained from the interpolation of the NURBS basis functions as follows:

$$\mathbf{x}\left(\xi, \eta, \zeta\right) = \sum_{I=1}^{n} \sum_{J=1}^{m} \sum_{K=1}^{l} R_{IJK}\left(\xi, \eta, \zeta\right) \bar{\mathbf{x}}_{IJK} \tag{11}$$

where

$$R_{IJK}\left(\xi, \eta, \zeta\right) = \frac{N_K^r\left(\zeta\right) N_I^q\left(\eta\right) N_J^p\left(\xi\right) W_{IJK}}{W} \tag{12}$$

The displacement $\mathbf{u}$ of a generic point in the solid-shell is the difference between its current ${}^{t+\Delta t}\mathbf{x}\left(\xi, \eta, \zeta\right)$ and reference ${}^{t}\mathbf{x}\left(\xi, \eta, \zeta\right)$ positions (Cardoso & Yoon, 2007):

$$\mathbf{u}\left(\xi, \eta, \zeta\right) = {}^{t+\Delta t}\mathbf{x}\left(\xi, \eta, \zeta\right) - {}^{t}\mathbf{x}\left(\xi, \eta, \zeta\right) = \sum_{I=1}^{n} \sum_{J=1}^{m} \sum_{K=1}^{l} R_{IJK}\left(\xi, \eta, \zeta\right) \bar{\mathbf{u}}_{IJK} \tag{13}$$

where $\bar{\mathbf{u}}_{IJK}$ represents the degrees of freedom at the control points IJK. The Cartesian linear strain tensor at any point can be described from the gradients of the displacement vector as follows:

$$\epsilon_{ij} = \frac{1}{2}\left(\frac{\partial u_i}{\partial x_j} + \frac{\partial u_j}{\partial x_i}\right) \tag{14}$$

The gradients of the displacement components are easily obtained by applying the chain rule to the NURBS approximations functions:

$$\frac{\partial u_i}{\partial x_j} = \frac{\partial R_{IJK} \cdot \bar{\mathbf{u}}_{IJK}}{\partial \xi_a} \frac{\partial \xi_a}{\partial x_j} \qquad \left(\xi_1 = \xi, \xi_2 = \eta, \xi_3 = \zeta\right) \tag{15}$$

where the expressions for the derivatives $\partial R_{IJK}/\partial \xi_a$ and $\partial \xi_a/\partial x_j$ are detailed in Appendix 1. Note that for the derivative $\partial \xi_a/\partial x_j$ the chain rule is applied between the derivatives of the physical coordinate system, the knot parametric space and the natural parametric space for Gaussian numerical integration (Cardoso & Cesar de Sa, 2012, 2014).

3.2. Virtual work and Incremental equations of motion

The equilibrium equations described in the current configuration, also known as the strong form, are described as follows:

$$\frac{\partial \sigma_{ij}}{\partial x_j} + f_i^B = 0 \tag{16}$$

where σ_{ij} are the Cauchy stress tensor components and f_i^B are the volumetric body forces. The natural (force) boundary conditions are expressed as:

$$\sigma_{ij} n_j = T_i \quad \text{on surface} \quad \Gamma \tag{17}$$

Considering an arbitrarily chosen continuous virtual displacement δu_i we can define the virtual work as follows:

$$\left(\frac{\partial \sigma_{ij}}{\partial x_j} + f_i^B \right) \delta u_i = 0 \tag{18}$$

and after integrating it by parts (weak form) over the entire domain of the body we get:

$$\int_v \sigma_{ij} \delta e_{ij} \, \mathrm{d}v = \int_v f_i^B \delta u_i \, \mathrm{d}v + \int_\Gamma T_i \delta u_i \, \mathrm{d}\Gamma \tag{19}$$

If we add the contribution of inertia terms to the virtual work from Equation (19) we obtain Newton's second law:

$$\int_v m_{ij} \ddot{u}_j \delta u_i \, \mathrm{d}v + \int_v \sigma_{ij} \delta e_{ij} \, \mathrm{d}v = \int_v f_i^B \delta u_i \, \mathrm{d}v + \int_\Gamma T_i \delta u_i \, \mathrm{d}\Gamma \tag{20}$$

or, after invoking the arbitrariness of the virtual displacement δu_i:

$$\mathbf{m} \cdot \ddot{\mathbf{u}} = \mathbf{F}^{ext.} - \mathbf{F}^{int.} \tag{21}$$

The internal force vector $\mathbf{F}^{int.}$ is obtained from the following virtual work term:

$$\mathbf{F}_{IJK}^{int.} \cdot \delta \mathbf{u}_{IJK} = \delta \mathbf{u}_{IJK}^T \cdot \int_v \mathbf{B}_{IJK}^T \cdot \boldsymbol{\sigma} \, \mathrm{d}v \tag{22}$$

or

$$\mathbf{F}_{IJK}^{int.} = \int_v \mathbf{B}_{IJK}^T \cdot \boldsymbol{\sigma} \, \mathrm{d}v \tag{23}$$

where the integral is performed for a volume domain between two consecutive knots along the parametric ξ, η and ζ directions. The strain–displacement matrix $\mathbf{B}_{IJK}$ is calculated from the derivatives of the NURBS basis functions as for example in Cardoso and Cesar de Sa (2012, 2014). Following the same

methodology described by Cardoso and Cesar de Sa (2014), the following strain–displacement matrix can be formulated for a particular integration point:

$$\mathbf{B}_{IJK} = \begin{bmatrix} \partial R_{IJK}/\partial x & 0 & 0 \\ 0 & \partial R_{IJK}/\partial y & 0 \\ 0 & 0 & \partial R_{IJK}/\partial z \\ \partial R_{IJK}/\partial y & \partial R_{IJK}/\partial x & 0 \\ \partial R_{IJK}/\partial z & 0 & \partial R_{IJK}/\partial x \\ 0 & \partial R_{IJK}/\partial z & \partial R_{IJK}/\partial y \end{bmatrix} \tag{24}$$

where the derivatives of the NURBS basis functions R_{IJK} are defined as in Equation (15) over the domain of influence (compact support) defined as $1 \leq I \leq p+1$, $1 \leq J \leq q+1$ and $1 \leq K \leq r+1$, with p, q and r defining the degree of the NURBS basis functions along ξ, η and ζ, respectively.

In this work the 3D formulation uses the B-bar approach for the treatment of the volumetric locking that might be present during the simulation of sheet metal forming processes. In this paper, the reduced integrated scheme according to Cardoso and Cesar de Sa (2014) is initially used at the IG 'element' for the calculation of the deviatoric strain components. This reduced integrated strain field is then projected into the full integration points by using the moving least square method. This technique has proved to deliver a deviatoric strain field that is free (or at least alleviated) from volumetric locking constraints.

3.3. Local constraints in IGA

The kinematic constraints in IGA can be imposed through the use of Lagrange multipliers in implicit time integration or through the use of a penalty parameter for explicit time integration schemes. For explicit time integration, the virtual work from Equation (20) is modified for the inclusion of generic local constraints through the use of a penalty multiplier as follows:

$$\int_v m_{ij}\ddot{u}_j \delta u_i \, \mathrm{d}v + \int_v \sigma_{ij}\delta e_{ij} \, \mathrm{d}v = \int_v f_i^B \delta u_i \, \mathrm{d}v + \int_\Gamma T_i \delta u_i \, \mathrm{d}\Gamma + \int_{\Gamma_c} \beta\delta\left(u_i - u^p\right) \, \mathrm{d}\Gamma_c \tag{25}$$

with β and u^p being the penalty multiplier and the prescribed displacement, respectively. Equation (25) is generic for local constraints in IGA and it can be used for the imposition of boundary conditions as well as for the zero penetration gap constraint for contact analysis in IGA.

4. Elastoplasticity and return mapping procedures

From a phenomenological point of view, the plastic flow can be interpreted as an irreversible process in a material body, typically a metal, characterised in terms of the history of the strain tensor $\boldsymbol{\epsilon}$ and two additional variables: the plastic strain $\boldsymbol{\epsilon}^p$ and a suitable set of internal variables generically denoted by

$\boldsymbol{\alpha}$ and often referred to as hardening parameters. Conventional constitutive laws which represent plastic deformation of metals are typically described by considering three parts: yield functions, stress–strain (or hardening) functions and the associative normality flow rule.

The yield function describes yield stresses in general deformation states, which are relative values measured with respect to a reference yield stress. A typical expression of the yield function is:

$$\phi = \phi(\boldsymbol{\sigma}, \boldsymbol{\alpha}) = \bar{\sigma}^m, \tag{26}$$

where ϕ, $\bar{\sigma}$ and $\boldsymbol{\sigma}$ are the yield function, the effective stress and the Cauchy stress tensor, respectively. The exponent m is a real number.

The stress–strain function represents the work-hardening behaviour of the reference stress, which is usually a uniaxial or balanced biaxial tension stress.

The notion of irreversibility of plastic flow is expressed by the following equations of evolution for the set of internal variables $\{\boldsymbol{\epsilon}^p, \boldsymbol{\alpha}\}$, called flow rule and hardening law:

$$\begin{aligned} {}^{\Delta t}\boldsymbol{\epsilon}^p &= \gamma \mathbf{r}(\boldsymbol{\sigma}, \boldsymbol{\alpha}) \\ {}^{\Delta t}\boldsymbol{\alpha} &= \gamma \mathbf{H}(\boldsymbol{\sigma}, \boldsymbol{\alpha}), \end{aligned} \tag{27}$$

where $\mathbf{r}(\boldsymbol{\sigma}, \boldsymbol{\alpha})$ and $\mathbf{H}(\boldsymbol{\sigma}, \boldsymbol{\alpha})$ are prescribed functions which define the direction of plastic flow and the type of hardening. The parameter γ is a nonnegative function, called the consistency parameter, which is assumed to obey the following Kuhn–Tucker complementary conditions:

$$\begin{aligned} \gamma &\geq 0 \\ f(\boldsymbol{\sigma}, \boldsymbol{\alpha}) &\leq 0 \\ \gamma f(\boldsymbol{\sigma}, \boldsymbol{\alpha}) &= 0, \end{aligned} \tag{28}$$

where $f(\boldsymbol{\sigma}, \boldsymbol{\alpha}) = \phi(\boldsymbol{\sigma}, \boldsymbol{\alpha}) - \bar{\sigma}^m$. In addition to conditions (28), there exists the consistency requirement:

$$\gamma \dot{f}(\boldsymbol{\sigma}, \boldsymbol{\alpha}) = 0. \tag{29}$$

The Kuhn–Tucker conditions can be interpreted as follows:

- suppose a specific state of stress and internal variables such that $f(\boldsymbol{\sigma}, \boldsymbol{\alpha}) < 0$ (elastic domain). Then, from the complementary condition $\gamma f(\boldsymbol{\sigma}, \boldsymbol{\alpha}) = 0$, γ is zero and consequently, ${}^{\Delta t}\boldsymbol{\epsilon}^p = 0$ and ${}^{\Delta t}\boldsymbol{\alpha} = 0$;
- now, suppose that the state of stress lays on the yield surface, that is, $f(\boldsymbol{\sigma}, \boldsymbol{\alpha}) = 0$. From the consistency requirement:
  - if $\dot{f}(\boldsymbol{\sigma}, \boldsymbol{\alpha}) < 0$, then $\gamma = 0$ and, consequently, unloading from a plastic state occurs;

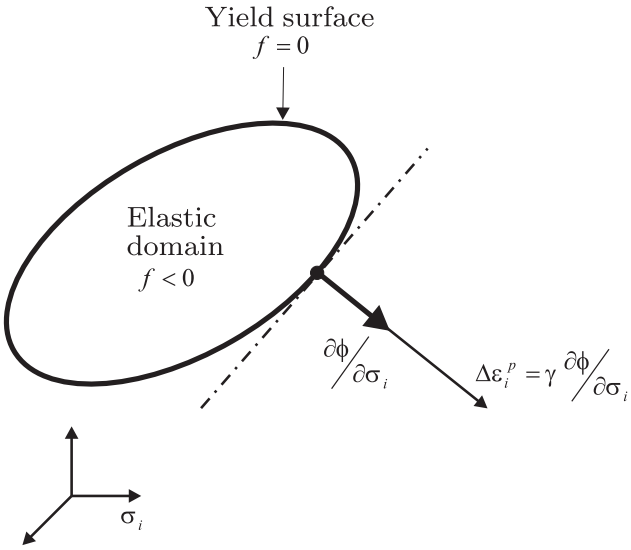

Figure 1. Loading/Unloading conditions and associative flow rule.

- if $\dot{f}(\boldsymbol{\sigma}, \boldsymbol{\alpha}) = 0$, then the consistency requirement is automatically satisfied. If $\gamma > 0$, then ${}^{\Delta t}\boldsymbol{\epsilon}^p \neq \mathbf{0}$ and ${}^{\Delta t}\boldsymbol{\alpha} \neq \mathbf{0}$, which gives plastic loading. If $\gamma = 0$, then a neutral loading state is obtained.

In the case of associative flow rule, the prescribed function $\mathbf{r}(\boldsymbol{\sigma}, \boldsymbol{\alpha})$ is obtained from the yield function ϕ:

$$\mathbf{r}(\boldsymbol{\sigma}, \boldsymbol{\alpha}) = \frac{\partial \phi}{\partial \boldsymbol{\sigma}}. \tag{30}$$

Figure 1 depicts the Kuhn–Tucker complementary conditions and the associative flow rule.

4.1. Stress update algorithms

The increment of the Cauchy stresses is obtained from the strain tensor as follows:

$${}^{\Delta t}\boldsymbol{\sigma} = \mathbf{D}\left({}^{\Delta t}\boldsymbol{\epsilon} - {}^{\Delta t}\boldsymbol{\epsilon}^p\right), \tag{31}$$

where ${}^{\Delta t}\boldsymbol{\sigma}$ is the incremental Cauchy stress tensor, $\mathbf{D}$ is the elastic matrix, ${}^{\Delta t}\boldsymbol{\epsilon}$ and ${}^{\Delta t}\boldsymbol{\epsilon}^p$ are the increments of the total and plastic deformations, respectively. The additive decomposition of the deformation gradient (Simo & Hughes, 1998) is used together with the co-rotational coordinate system so that incremental objectivity is ensured for large deformations. The co-rotational approach has been used extensively in the past (Cardoso, 2002; Cardoso & Yoon, 2005; Yoon et al., 1999) and it is very common for the modelling of large deformations in shell-like structures such as the ones used in sheet metal forming applications. Other

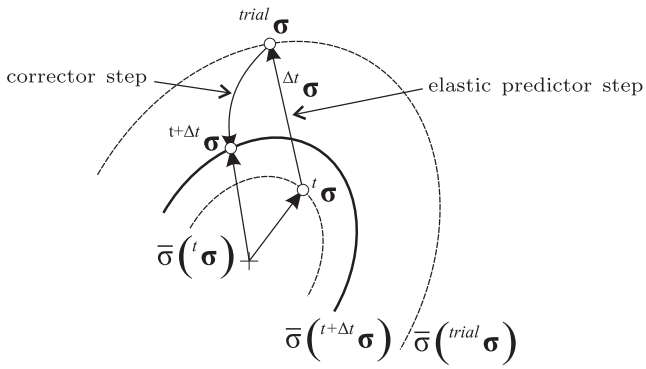

Figure 2. Predictor-corrector algorithm for elastoplastic materials.

worth considering research for large deformations is the use of the multiplicative decomposition of the deformation gradient, with the pioneer work of Simo and Hughes (1998) and, more recently, with the works of Deseri and Owen (2002, 2016).

Figure 2 illustrate the incremental application of elastoplasticity. The procedure described in Figure 2 follows two steps:

- *elastic predictor* step; Equation (31) is used to obtain the incremental components of the Cauchy stresses and to define the elastic trial state as ${}^{trial}\boldsymbol{\sigma} = {}^{t}\boldsymbol{\sigma} + {}^{\Delta t}\boldsymbol{\sigma}$;
- *plastic corrector* step; Considering Equation (27) and associative flow rule, the final state corresponding to ${}^{t+\Delta t}\boldsymbol{\sigma}$ is obtained from the trial state:

$$\begin{aligned} {}^{t+\Delta t}\boldsymbol{\sigma} &= {}^{trial}\boldsymbol{\sigma} - \mathbf{D}\,{}^{\Delta t}\boldsymbol{\epsilon}^{p} = {}^{trial}\boldsymbol{\sigma} - \gamma\mathbf{D}\frac{\partial\bar{\sigma}\left({}^{t+\alpha\Delta t}\boldsymbol{\sigma}\right)}{\partial\boldsymbol{\sigma}} \\ &= {}^{trial}\boldsymbol{\sigma} - \gamma\mathbf{D}\left({}^{t+\alpha\Delta t}\mathbf{m}\right), \end{aligned} \tag{32}$$

where ${}^{t+\alpha\Delta t}\mathbf{m}$ represents the normal to the yield surface at a representative point $t + \alpha\Delta t$, with $0 \leq \alpha \leq 1$. From work plastic equivalence and proportional loading:

$${}^{\Delta t}\bar{\epsilon}^{p} = \frac{{}^{t+\alpha\Delta t}\boldsymbol{\sigma} : {}^{\Delta t}\boldsymbol{\epsilon}^{p}}{\bar{\sigma}\left({}^{t+\alpha\Delta t}\boldsymbol{\sigma}\right)} = \frac{{}^{t+\alpha\Delta t}\boldsymbol{\sigma} : \gamma\dfrac{\partial\bar{\sigma}\left({}^{t+\alpha\Delta t}\boldsymbol{\sigma}\right)}{\partial\boldsymbol{\sigma}}}{\bar{\sigma}\left({}^{t+\alpha\Delta t}\boldsymbol{\sigma}\right)} = \frac{\gamma\bar{\sigma}\left({}^{t+\alpha\Delta t}\boldsymbol{\sigma}\right)}{\bar{\sigma}\left({}^{t+\alpha\Delta t}\boldsymbol{\sigma}\right)} = \gamma \tag{33}$$

where ${}^{\Delta t}\bar{\epsilon}^{p}$ is the equivalent plastic strain increment.

4.1.1. Numerical implementation

In the numerical procedure, the unknown ${}^{\Delta t}\bar{\epsilon}^{p}$ (equivalent plastic strain increment) is obtained from the non-linear equations, which are derived in the formulation. Using ${}^{\Delta t}\bar{\epsilon}^{p}$ obtained from the non-linear equation, all variables on kinematics and stresses are updated at the end of every step. The non-linear

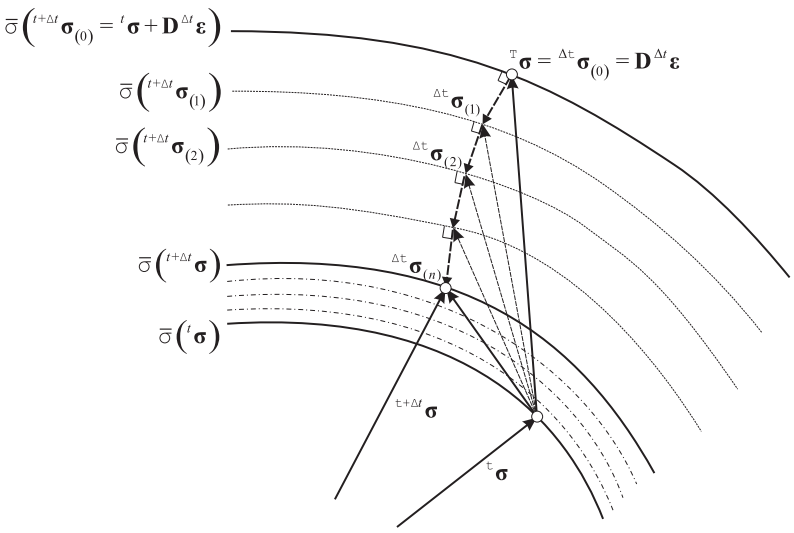

Figure 3. Schematic representation of the iterative solving procedure for return mapping.

equation to solve for ${}^{\Delta t}\bar{\epsilon}^{p}$, which enables the resulting stresses to stay on the hardening curve is:

$$\phi\left({}^{t}\boldsymbol{\sigma} + {}^{\Delta t}\boldsymbol{\sigma}\right)^{\frac{1}{m}} = \rho\left({}^{t}\bar{\epsilon}^{p} + {}^{\Delta t}\bar{\epsilon}^{p}\right). \tag{34}$$

The semi-implicit multi-stage return mapping procedure from Yoon et al. (1999) is employed. Note that in the incremental deformation theory ${}^{\Delta t}\bar{\epsilon}^{p} = \gamma$ and $\phi^{\frac{1}{m}}\left(\boldsymbol{\sigma}\right) = \bar{\sigma}\left(\boldsymbol{\sigma}\right)$.

In the semi-implicit multi-stage return mapping procedure the following residual is present for each stage I:

$$R = \bar{\sigma}\left({}^{t}\boldsymbol{\sigma} + {}^{\Delta t}\boldsymbol{\sigma}_{(I)}\right) - \rho\left({}^{t}\bar{\epsilon}^{p} + \gamma_{(I)}\right) = R_I, \tag{35}$$

or

$$\psi = \bar{\sigma}\left({}^{t}\boldsymbol{\sigma} + {}^{\Delta t}\boldsymbol{\sigma}_{(I)}\right) - \rho\left({}^{t}\bar{\epsilon}^{p} + \gamma_{(I)}\right) - R_I = 0. \tag{36}$$

In order to solve Equation (36), the following definitions are summarised:

$$\begin{aligned} &\text{(i)} \quad {}^{\Delta t}\boldsymbol{\sigma} = \mathbf{D}\left({}^{\Delta t}\boldsymbol{\epsilon} - {}^{\Delta t}\boldsymbol{\epsilon}^{p}\right) = \mathbf{D}\,{}^{\Delta t}\boldsymbol{\epsilon} - \gamma\mathbf{D}\frac{\partial\bar{\sigma}}{\partial\boldsymbol{\sigma}} \\ &\text{(ii)} \quad {}^{trial}\boldsymbol{\sigma} = {}^{t}\boldsymbol{\sigma} + \mathbf{D}\,{}^{\Delta t}\boldsymbol{\epsilon} = {}^{t}\boldsymbol{\sigma} + \mathbf{D}\,{}^{\Delta t}\boldsymbol{\epsilon}. \end{aligned} \tag{37}$$

The linearisation of Equation (36) leads to:

$$\psi_0 + \frac{\partial\psi}{\partial\,{}^{t+\Delta t}\boldsymbol{\sigma}_{(I-1)}}\,d\,{}^{\Delta t}\boldsymbol{\sigma}_{(I)} + \frac{\partial\psi}{\partial\rho}\,d\rho = 0, \tag{38}$$

where

$$\psi_0 = \bar{\sigma}\left({}^{t}\boldsymbol{\sigma} + {}^{\Delta t}\boldsymbol{\sigma}_{(I-1)}\right) - \rho\left({}^{t}\bar{\epsilon}^{p} + \gamma_{(I-1)}\right) - R_I = 0. \tag{39}$$

Considering the relations $\dfrac{\partial\psi}{\partial\, {}^{t+\Delta t}\boldsymbol{\sigma}_{(I-1)}} = \dfrac{\partial\bar{\sigma}}{\partial\, {}^{t+\Delta t}\boldsymbol{\sigma}_{(I-1)}}$ and also $\dfrac{\partial\psi}{\partial\rho} = -1$, Equation (38) becomes:

$$\psi_0 + \frac{\partial\bar{\sigma}}{\partial\, {}^{t+\Delta t}\boldsymbol{\sigma}_{(I-1)}}\, d\, {}^{\Delta t}\boldsymbol{\sigma}_{(I)} - d\rho = 0. \tag{40}$$

From Equation (37):

$$\begin{aligned} &\text{(i)} \quad d\, {}^{\Delta t}\boldsymbol{\sigma}_{(I)} = -\mathrm{d}\gamma_{(I)}\mathbf{D}\frac{\partial\bar{\sigma}}{\partial\, {}^{t+\Delta t}\boldsymbol{\sigma}_{(I-1)}} \\ &\text{(ii)} \quad d\rho = \mathrm{d}\gamma_{(I)}H. \end{aligned} \tag{41}$$

In the semi-implicit algorithm the evaluation of the second-order derivatives, $\frac{\partial}{\partial\boldsymbol{\sigma}}\left(\frac{\partial\bar{\sigma}}{\partial\boldsymbol{\sigma}}\right)$ is not necessary because the normal to the yield surface, $\frac{\partial\bar{\sigma}}{\partial\boldsymbol{\sigma}}$ is assumed from the previous stage $(I-1)$.

In Equation (41), $H \equiv \frac{\mathrm{d}\bar{\sigma}}{\mathrm{d}\bar{\epsilon}^{p}}$ comes directly from the uniaxial stress–strain curve. Substituting Equation (41) into Equation (40) gives:

$$\psi_0 - \mathrm{d}\gamma_{(I)}\frac{\partial\bar{\sigma}}{\partial\, {}^{t+\Delta t}\boldsymbol{\sigma}_{(I-1)}}\mathbf{D}\frac{\partial\bar{\sigma}}{\partial\, {}^{t+\Delta t}\boldsymbol{\sigma}_{(I-1)}} - \mathrm{d}\gamma_{(I)}H = 0. \tag{42}$$

By considering the normal to the yield surface for stage $(I-1)$:

$${}^{t+\Delta t}\mathbf{m}_{(I-1)} = \frac{\partial\bar{\sigma}}{\partial\, {}^{t+\Delta t}\boldsymbol{\sigma}_{(I-1)}}, \tag{43}$$

the following result for $\mathrm{d}\gamma_{(I)}$ is obtained:

$$\mathrm{d}\gamma_{(I)} = \frac{\psi_0}{\left({}^{t+\Delta t}\mathbf{m}_{(I-1)}\right)\mathbf{D}\left({}^{t+\Delta t}\mathbf{m}_{(I-1)}\right) + H}. \tag{44}$$

The update of the variables is next performed:

$$\begin{aligned} \gamma_{(I)} &= \gamma_{(I-1)} + \mathrm{d}\gamma_{(I)} \\ {}^{\Delta t}\boldsymbol{\sigma}_{(I)} &= {}^{\Delta t}\boldsymbol{\sigma}_{(I-1)} - \mathrm{d}\gamma_{(I)}\mathbf{D}\frac{\partial\bar{\sigma}}{\partial\, {}^{t+\Delta t}\boldsymbol{\sigma}_{(I-1)}} \\ {}^{t+\Delta t}\boldsymbol{\sigma}_{(I)} &= {}^{t}\boldsymbol{\sigma} + {}^{\Delta t}\boldsymbol{\sigma}_{(I)}. \end{aligned} \tag{45}$$

Note that ${}^{\Delta t}\boldsymbol{\sigma}_{(0)} = \mathbf{D}\, {}^{\Delta t}\boldsymbol{\epsilon}$. In Figure 3, a schematic representation of the return mapping procedure for the semi-implicit algorithm is presented. It is possible

to see that the normal to the yield surface is calculated on the previous stage $(I-1)$, and, consequently its direction is known on the current stage (I). The return mapping procedure in Figure 3 is described in Box 1.

In the semi-implicit scheme, the normal to the yield surface is evaluated explicitly (its direction is calculated on previous stage) while the consistency parameter $\mathrm{d}\gamma$ is evaluated implicitly at current stage (I). It is possible to use more sophisticated scheme like Euler-backward method. In this case, both normal to the yield surface and consistency parameter are evaluated implicitly at current stage (I). Yoon et al. (1999) developed an iterative solving scheme based on the fully implicit stress update algorithm. The algorithm was successfully applied to a non-quadratic yield function and a general hardening law.

Box1-Multi-stage return mapping procedure.

0. $I = 1$; $\gamma_{(0)} = 0$; ${}^{t+\Delta t}\boldsymbol{\sigma}_{(0)} = {}^{trial}\boldsymbol{\sigma}$; $n =$ number of stages

1. Cycle on n:

$$- \psi\left(\gamma_{(I-1)}\right) = \bar{\sigma}\left({}^{t+\Delta t}\boldsymbol{\sigma}_{(I-1)}\right) - \rho\left({}^{t}\bar{\epsilon}^{p}\right) = \psi_{(I-1)}$$

$$- {}^{t+\Delta t}\mathbf{m}_{(I-1)} = \frac{\partial\bar{\sigma}}{\partial\, {}^{t+\Delta t}\boldsymbol{\sigma}_{(I-1)}}$$

$$- \mathrm{d}\gamma_{(I)} = \frac{\psi_{(I-1)}}{\left({}^{t+\Delta t}\mathbf{m}_{(I-1)}\right)\mathbf{D}\left({}^{t+\Delta t}\mathbf{m}_{(I-1)}\right) + H}$$

$$- \gamma_{(I)} = \gamma_{(I-1)} + \mathrm{d}\gamma_{(I)}$$

$$- {}^{\Delta t}\boldsymbol{\sigma}_{(I)} = {}^{\Delta t}\boldsymbol{\sigma}_{(I-1)} - \mathrm{d}\gamma_{(I)}\mathbf{D}\frac{\partial\bar{\sigma}}{\partial\, {}^{t+\Delta t}\boldsymbol{\sigma}_{(I-1)}}$$

$$- {}^{t+\Delta t}\boldsymbol{\sigma}_{(I)} = {}^{t}\boldsymbol{\sigma} + {}^{\Delta t}\boldsymbol{\sigma}_{(I)}$$

$$- I = I + 1$$

5. Contact procedures in IGA

The consideration of contact procedures is fundamental for the numerical simulation for manufacturing processes such as sheet metal forming. In order to achieve a reliable and efficient numerical simulation with contact in finite element analysis, three major steps need to be considered: (1) the global search phase,

where a first search is performed such that potential contact nodes are associated with a target contact face; (2) the local search step, where the exact location of the contact point on the target face is determined; (3) the imposition of the zero-penetration gap (local constraint) in the weak formulation. Contact analysis in IGA also has to include these three major steps but additional challenges are encountered due to the non-interpolatory characteristic of the method. Nevertheless, there are however some important benefits of contact in IGA such as the higher degree of the polynomials in the NURBS basis functions, which enables the contact to be smoother leading to higher convergence rates, and the fact that it does not use element subdivisions, which in turn does not introduce inter-element discontinuity when a contact node travels between adjacent elements as in the finite element method. An outline of the major steps that are considered for the implementation of contact procedures in IGA are detailed in the following sections.

In Figure 4 (b) it can be clearly seen the non-interpolatory nature of NURBS in such that the control points (represented by the white circles in the figure) are not in the curve. Instead, the dark squares in the figure represent the coordinates of a point in the curve after being approximated by the basis functions from Equation (7) from a knot value defined in the parametric space of the knot vectors.

For contact search/detection it is fundamental that the algorithm goes through the physical coordinates on the curve rather than through the control net. For example, the calculation of the gap (see Figure 5) needs to be done from the detection of penetration between points in the curves/surfaces rather than the control points on their control nets. Due to the non-interpolatory character of NURBS, special methods, such as point inversion (Piegl & Tiller, 1996) for the determination of the parametric knot coordinates corresponding to a minimum distance to a contacting point, need to be used.

In this work, the Master–Slave contact scheme was implemented with the rigid contact surfaces for the dies being the master surfaces, while the contact surfaces for the deformable blank sheet being the slave contact surfaces.

5.1. Global search

Global contact search is the phase in contact mechanics where hitting nodes (knots in IGA) are searched within the vicinity of a target contact surface. A target contact face in IGA is defined as a face between two consecutive knots, ξ_i and ξ_{i+1} along the ξ direction and η_i and η_{I+1} along the η direction. Global search does a first selection of the potential hitting nodes in the territory domain of a target contact face and thereafter the local search accurately determines the point at the target surface that corresponds to the minimum distance to the hitting node.

The first stage in the global search procedure for IGA is the use of the position code algorithm Oldenburg and Nilsson (1994) and Cardoso (2002), where the domain is divided into three-dimensional cube boxes with each having

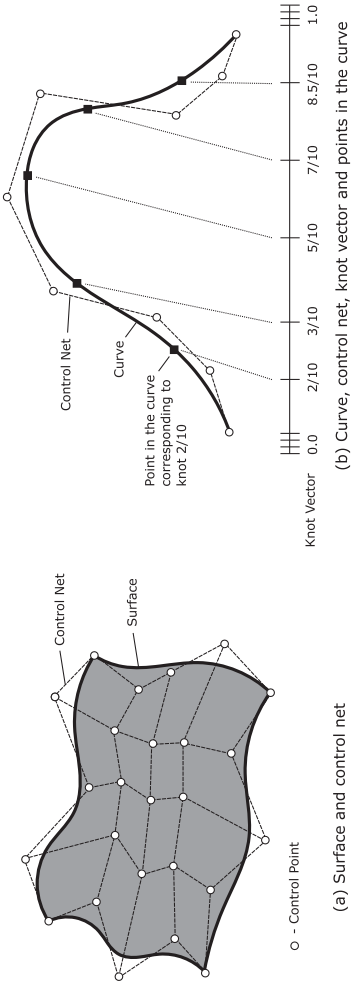

Figure 4. Definitions for control points, control net and knot vector. (a) NURBS surface and its control net. (b) 2D curve with its control points, knot vector in the parametric space and points in the curve after approximation with NURBS basis functions.

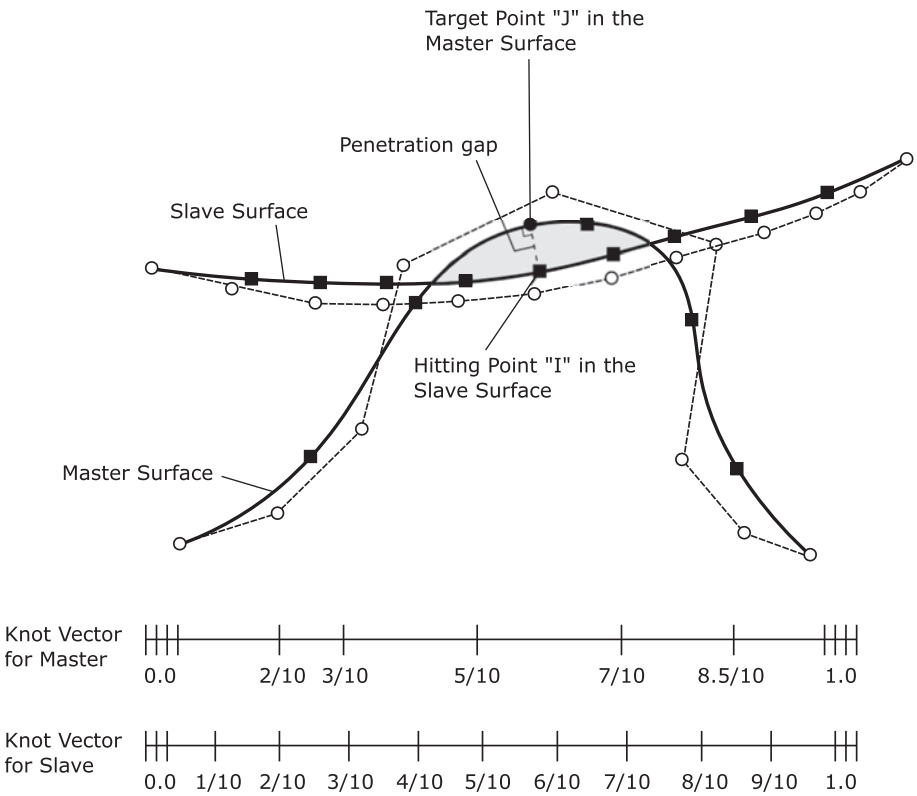

Figure 5. Contact detection between a master surface (rigid dies) and a slave surface (deformable blank sheet).

an associated integer number. Whenever the coordinates of a knot, whether it is a target or hitting knot in IGA, lies inside any of these three-dimensional boxes then it is assigned a unique integer. The position code algorithm then performs a binary search (Cardoso, 2002) and selects the knots inside the contact territory of the target contact surface (red domain defined in Figure 6). Depending on the size of the three-dimensional boxes used in the position code algorithm, there could be the possibility of having knots that can be considered to be within the contact territory domain of a target contact face but in fact they might not be. It is therefore important to have a very precise selection of knots inside the contact territory of each contact face otherwise the local contact search procedure for the calculation of the precise location of the target contact coordinates can be very time consuming. Figure 6 details a second filter that is used for a better selection of knots inside the contact territory for IGA contact analysis. The hitting knots inside the contact territory of a target NURBS contact face are given from the intersection of the following sub-sets:

$$\begin{aligned} A = & \quad \left\{ \mathbf{x}_A \in I\!R : \left(\mathbf{V}_{i-j} \times \mathbf{V}_{i-h} \right) \cdot \mathbf{V}_{ni} \geq 0, \quad \left(i = 1,2,3,4\,;\; j = 2,3,4,1 \right) \right\} \\ B = & \left\{ \mathbf{x}_B \in I\!R : \left(\mathbf{V}_{k-l} \times \mathbf{V}_{k-h} \right) \cdot \mathbf{V}_{nk} \geq 0, \quad \left(k = 1,5,8,4\,;\; l = 5,8,4,1 \right) \right\} \end{aligned} \tag{46}$$

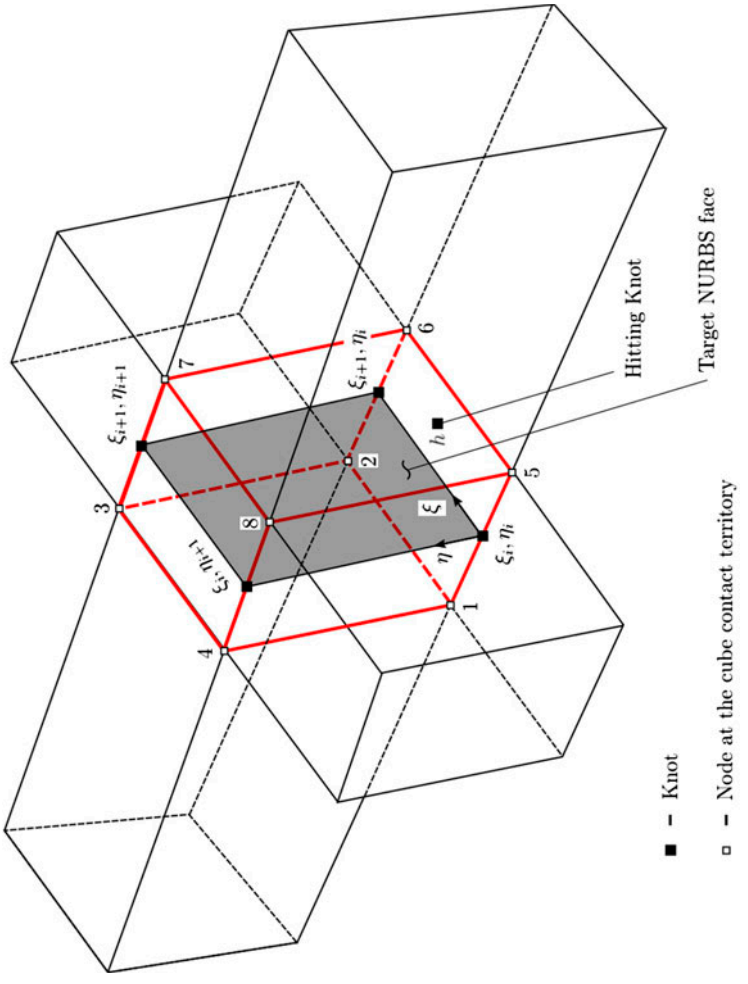

Figure 6. Contact territory of one NURBS contact face.

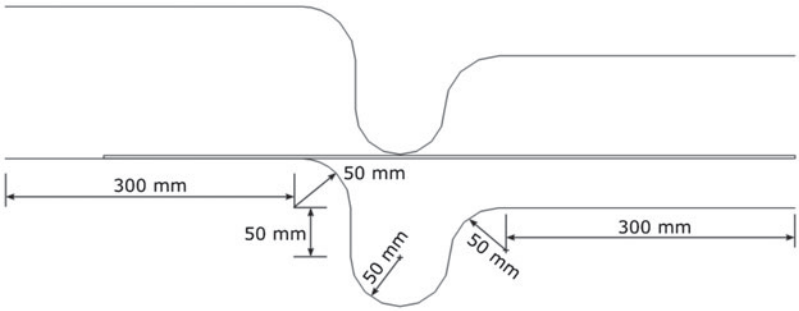

Figure 7. Geometry and dimensions for the lower-die tool.

i.e.

$$C = A \cap B \tag{47}$$

with C defining the set of hitting knots inside the contact territory of a target NURBS contact face. $\mathbf{V}_{i-j}$ is the vector connecting two consecutive vertices on the contact territory cube, $\mathbf{V}_{ni}$ is the normal vector of the face on the cube contact territory and $\mathbf{V}_{i-h}$ is the vector connecting the hitting knot with the vertex of the contact territory cube. With this second filter the resolution error that might be existent during the construction of the three-dimensional boxes for the position code algorithm is eliminated and thus a more accurate selection of knots in the contact territory can be obtained.

5.2. Local search and penetration gap

The NURBS contact surfaces $\mathbf{S}(\xi, \eta)$ are defined from the NURBS approximation as defined in Equation (7). The aim of local search procedures is to determine the exact location of the parametric NURBS coordinates ξ and η corresponding to the minimum distance to the hitting point (hitting knot) located inside the contact territory of a target contact face. Assuming an initial guess for the parametric coordinates of the NURBS surface, $\xi = \xi_0$ and $\eta = \eta_0$, the following position vector can be defined:

$$\mathbf{r}(\xi, \eta) = \mathbf{x}_h - \mathbf{S}(\xi, \eta) \tag{48}$$

where $\mathbf{x}_h$ are the coordinates of the hitting knot. The parametric coordinates ξ and η that minimise the distance to the hitting knot are obtained from imposing the following dot product equal to zero:

$$\begin{aligned} f(\xi, \eta) &= \mathbf{S}_\xi(\xi, \eta) \cdot \mathbf{r}(\xi, \eta) = 0 \\ h(\xi, \eta) &= \mathbf{S}_\eta(\xi, \eta) \cdot \mathbf{r}(\xi, \eta) = 0 \end{aligned} \tag{49}$$

The Newton–Raphson iterative scheme is then used for the solution of the nonlinear system from Equations (49) after their development into the following

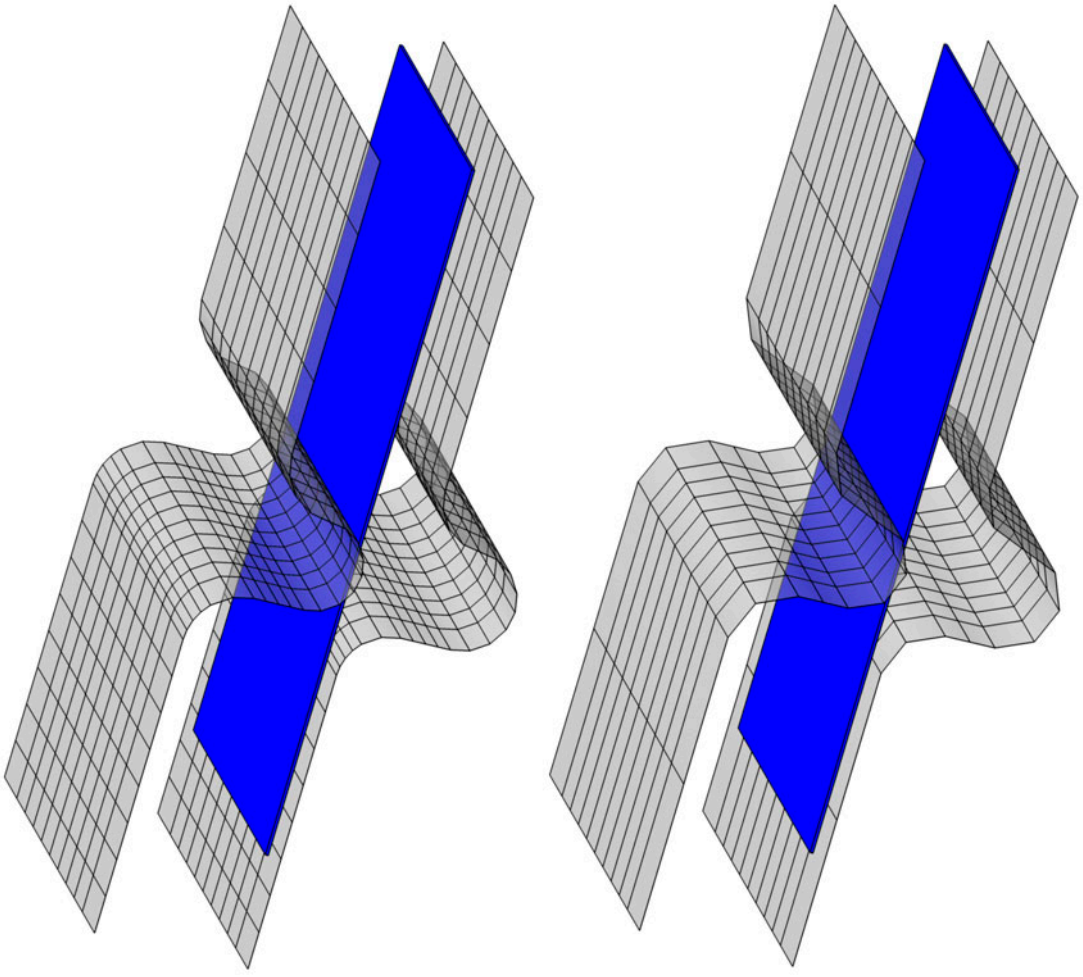

Figure 8. Knot distribution for the NURBS die tools: upper tool set - refined knot distribution; lower tool set - coarse knot distribution.

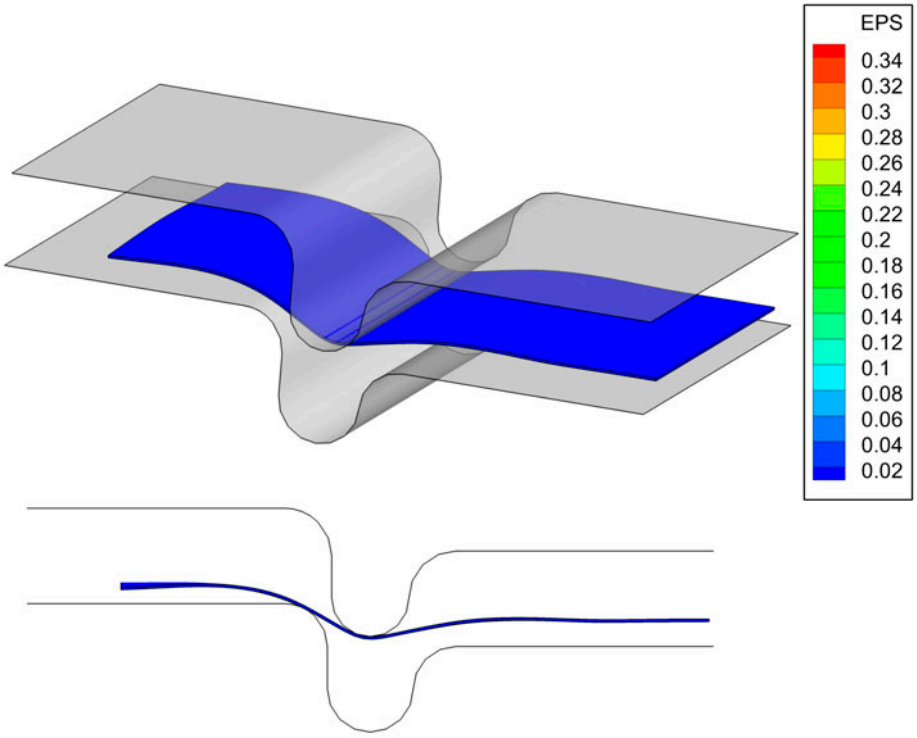

Figure 9. First plot for an intermediate time step for the refined tool set. 3D view with the distribution of the equivalent plastic strain (EPS) and profile view for contact validation.

Taylor's series:

$$\mathbf{F}^{i+1}(\xi,\eta) = \mathbf{F}^{i}(\xi,\eta) + \frac{d\mathbf{F}(\xi,\eta)}{d\mathbf{u}}\Delta\mathbf{u} + \text{H.O.T.} \tag{50}$$

with

$$\mathbf{F}(\xi,\eta) = \begin{Bmatrix} f(\xi,\eta) \\ h(\xi,\eta) \end{Bmatrix} \quad ; \quad \mathbf{u} = \begin{Bmatrix} \xi \\ \eta \end{Bmatrix} \tag{51}$$

Because the aim is to have $\mathbf{F}^{i+1}(\xi,\eta) = \mathbf{0}$, the linear system of equations that needs to be solved for is:

$$\begin{bmatrix} f_\xi(\xi,\eta) & f_\eta(\xi,\eta) \\ h_\xi(\xi,\eta) & h_\eta(\xi,\eta) \end{bmatrix} \begin{Bmatrix} \Delta\xi \\ \Delta\eta \end{Bmatrix} = -\begin{Bmatrix} f^i(\xi,\eta) \\ h^i(\xi,\eta) \end{Bmatrix} \tag{52}$$

After having the increment of the parametric knot coordinates, the current knot coordinates can be updated as follows:

$$\begin{aligned} \xi^{i+1} &= \xi^i + \Delta\xi \\ \eta^{i+1} &= \eta^i + \Delta\eta \end{aligned} \tag{53}$$

After the convergence of the above Newton–Raphson scheme for the knot coordinates of the point on the target NURBS face with the shortest distance

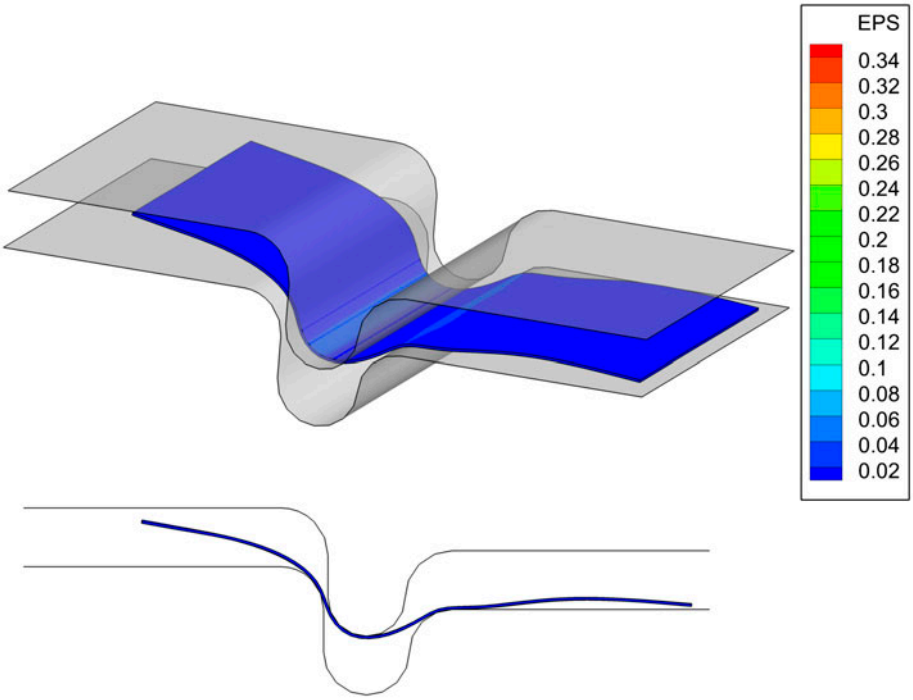

Figure 10. Second plot for an intermediate time step for the refined tool set. 3D view with the distribution of the equivalent plastic strain (EPS) and profile view for contact validation.

to the hitting knot, the penetration gap, $g\left(\xi,\eta\right)$, can thus be calculated from the use of the NURBS basis functions as follows:

$$g\left(\xi^{i+1},\eta^{i+1}\right)=\left(\mathbf{x}_h-\mathbf{S}\left(\xi^{i+1},\eta^{i+1}\right)\right)\cdot\mathbf{V}_n\left(\xi^{i+1},\eta^{i+1}\right) \tag{54}$$

where $\mathbf{V}_n\left(\xi^{i+1},\eta^{i+1}\right)$ is the unit normal vector at the contact knot in the target NURBS surface and it is given by:

$$\mathbf{V}_n\left(\xi^{i+1},\eta^{i+1}\right)=\frac{\frac{d\mathbf{S}\left(\xi^{i+1},\eta^{i+1}\right)}{d\xi^{i+1}}\times\frac{d\mathbf{S}\left(\xi^{i+1},\eta^{i+1}\right)}{d\eta^{i+1}}}{\left\|\frac{d\mathbf{S}\left(\xi^{i+1},\eta^{i+1}\right)}{d\xi^{i+1}}\times\frac{d\mathbf{S}\left(\xi^{i+1},\eta^{i+1}\right)}{d\eta^{i+1}}\right\|} \tag{55}$$

As can be seen from the Newton–Raphson iterative scheme above, it is fundamental to have in the global search a narrow selection of potential hitting knots inside the contact territory of a target IG contact face, otherwise the local search in IGA can be very time consuming. Also, and even more critical, is the fact that in the Newton–Raphson scheme defined above it is quite critical to have a very good initial guess for ξ_0 and η_0 so that the iterative scheme converges quickly and does not diverge. The initial guesses used in this work for ξ_0 and η_0 are the knot parametric coordinates ξ_i and η_i from the contact target face in Figure 6 which defines the contact territory of the hitting knot.

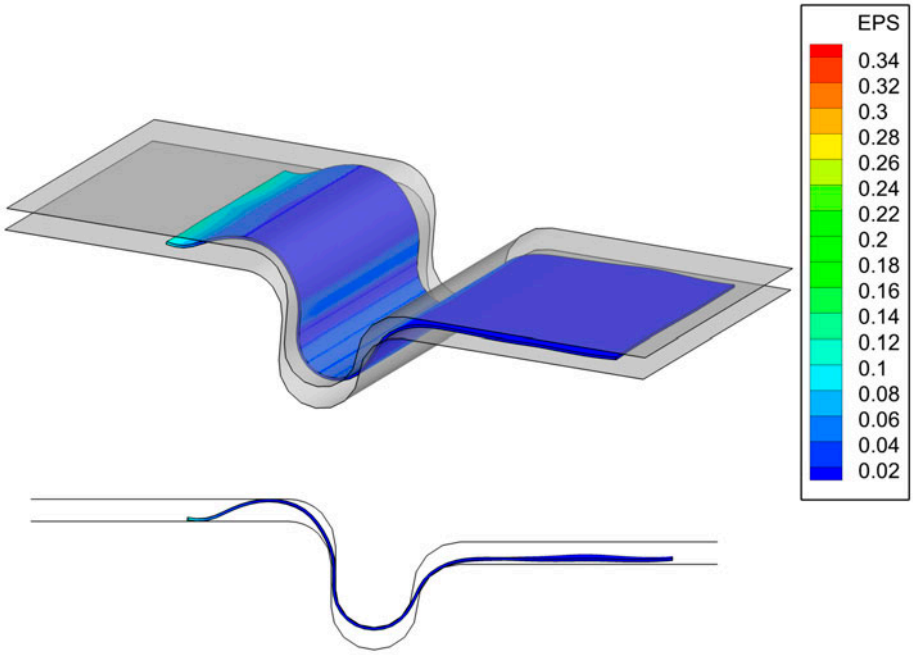

Figure 11. Third plot for an intermediate time step for the refined tool set. 3D view with the distribution of the equivalent plastic strain (EPS) and profile view for contact validation.

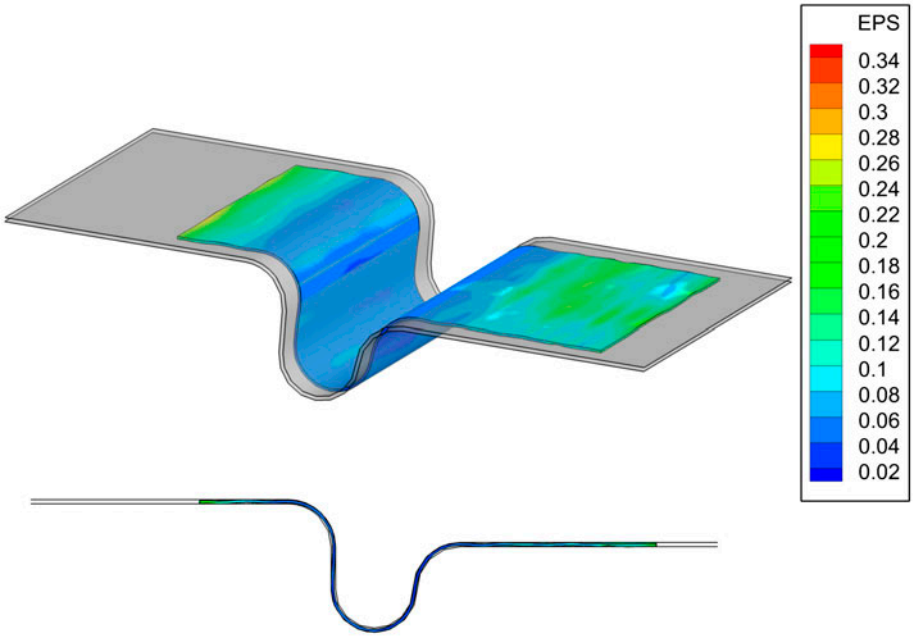

Figure 12. Fourth plot for the final time step for the refined tool set. 3D view with the distribution of the equivalent plastic strain (EPS) and profile view for contact validation.

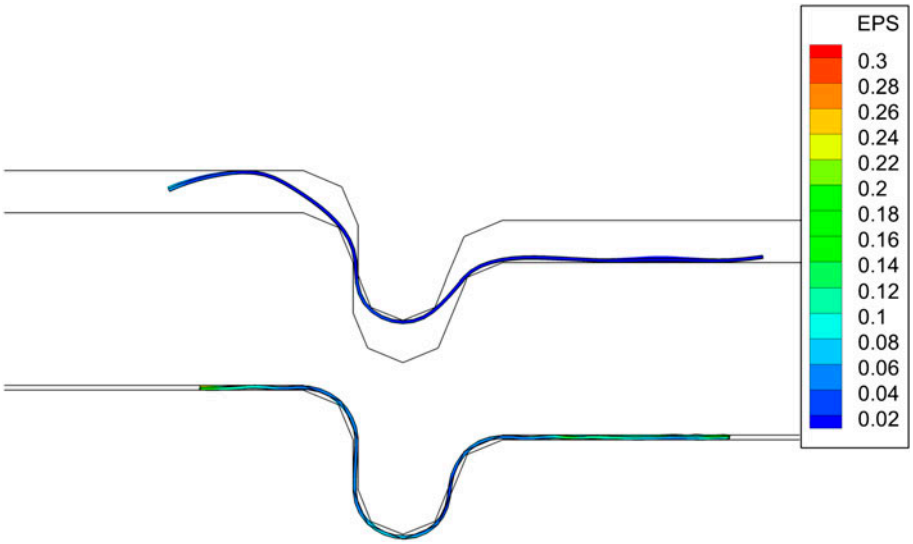

Figure 13. Two profile plots for the coarser tool set: (1) intermediate step; (2) final time step.

6. Numerical results

The numerical results presented here demonstrate the contact capabilities of the IsoGeometric analysis in a sheet metal forming application. The simulation includes two rigid dies based on NURBS surfaces: a lower die, with geometry and dimensions described in Figure 7 and an upper die, which was offset by 5 mm from the lower die. The lower die moves in the vertical upward direction with a velocity of 18.75 m/s while the upper die moves in the vertical downward direction with a velocity of −18.75 m/s.

The blank sheet has 700 mm length, 400 mm width and 3.0 mm thickness and it was modelled with 3D IGA 'elements' (with each IGA 'element' defined between two consecutive knots) with degree 2 in the NURBS basis functions. The material elastic properties used for the simulation were Young's modulus equal to 210 GPa and Poisson's ratio equal to .3. The Voce hardening rule was used with the following hardening parameters:

$$\bar{\sigma} = 500.0 - 250.0 \times \exp\left(-6.0 \times \bar{\epsilon}^{p}\right)$$

and the classical von-Mises yield function was used for the elastoplastic return mapping procedure. It is worth pointing out that the main objective of this simulation is to validate the IsoGeometric analysis with contact rather than detailed elastoplasticity analysis.

Figure 8 depicts the two options used for the geometric description of the NURBS rigid die tools. The figure at the top represents the refined die tool sets where a higher number of knots were used to represent the geometry of the NURBS surface, whilst the figure at the bottom shows a coarser representation of the die tools by using a smaller number of knots in the NURBS surface. These

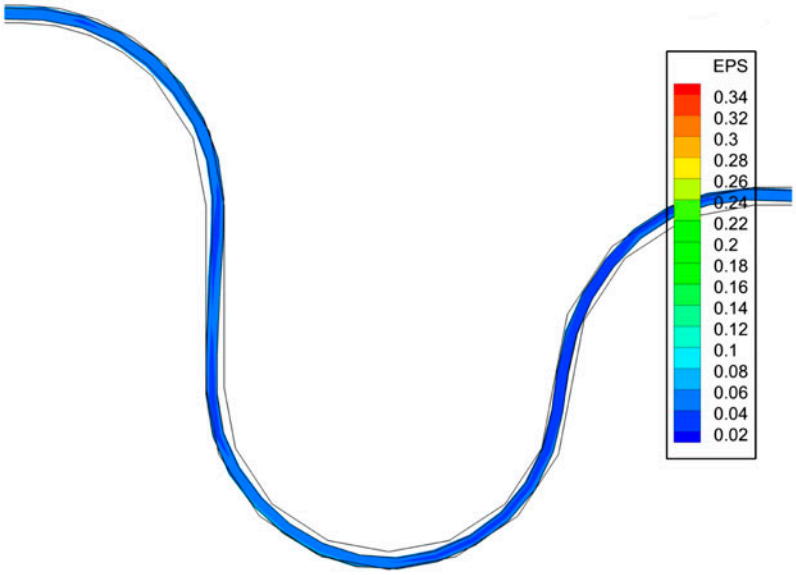

(a) Refined tool set.

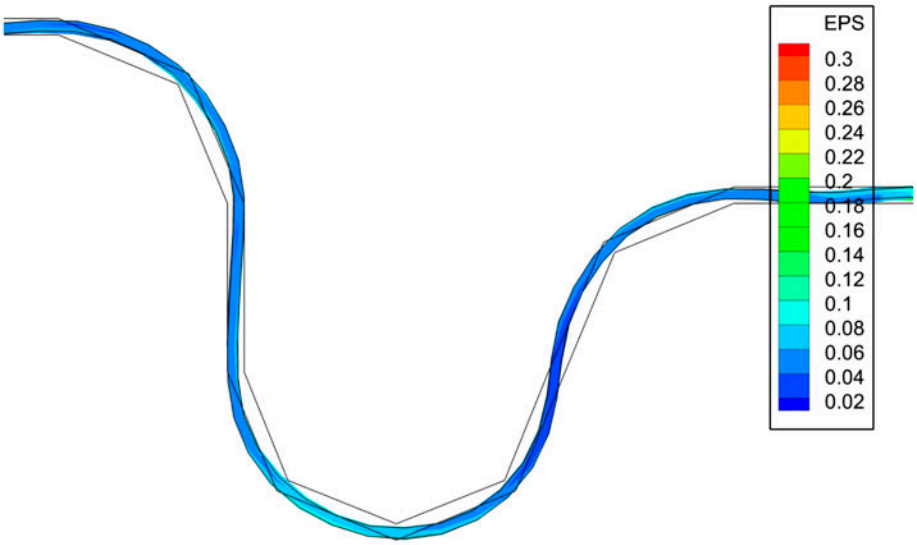

(b) Coarse tool set.

Figure 14. Zoom-in for the final time step for both the refined and coarser tool sets.

two different geometric representations were used separately for the numerical simulation of contact procedures in the IGA of sheet metal forming processes. In Appendix 2, Tables B1–B3, give the distribution of the control points and knot vectors used for both die tools.

Figures 9–12 describe the deformed configuration of the blank sheet for a sequence of different time steps during the forming analysis and for the refined

tool set. In these figures, the 3D perspective view with the distribution of the equivalent plastic strain (EPS in the contour legend) is shown as well as a profile view of the forming process.

In Figure 13, an intermediate step and the final forming step for the IGA simulation using the coarser die tool set are shown. The objective of this simulation is to demonstrate that the same forming results can be obtained with a tool set with a much smaller distribution of knots in the NURBS rigid surfaces. This offers enormous computational efficiencies during global search and local search procedures for IGA contact analysis and hence it demonstrates the advantages of IGA in sheet metal forming simulations.

Figure 14(a) and (b) show a zoomed-in of the regions with higher curvature for both the refined and coarse representation of the dies for the final time step. As can be clearly seen, the same accurate final geometric deformed shape can be obtained when the coarse distribution of knots in the rigid die sets is used.

7. Concluding remarks

In this work contact procedures for IsoGeometric Analysis were developed for the simulation of sheet metal forming processes. Both the rigid tools and the deformable blank sheet were approximated with NURBS basis functions under the framework of IGA. Global and local search procedures were developed for the detection of potential contact knots between the NURBS defined contact surfaces. Some additional difficulties encountered for contact detection in IGA and, more importantly the need for an accurate description (initial guess) of potential contact knots during the global search phase so that the iterative Newton–Raphson scheme for the exact location of the target parametric coordinates would not encounter any convergence difficulties, were discussed in this paper. It was however shown that the advantages of modelling the entire sheet metal forming process with IGA largely overcome these minor difficulties. Such advantages include: (1) the possibility of using very coarse distribution of knots in the rigid NURBS surfaces, thereby allowing faster contact analysis; (2) the possibility of using higher order polynomials to describe the NURBS geometry, thereby allowing for an even smaller number of knots to be considered without the disruption of the geometry of the contact surfaces; (3) smoother contact due to the lack of inter-element discontinuity whenever a contact node travels between adjacent knot spans; (4) the use of larger critical time steps in explicit analyses due to the coarser distribution of knots.

The numerical sheet metal-forming example presented in this paper demonstrates all the above-mentioned advantages of using IGA for the numerical simulation of sheet metal-forming processes.

Disclosure statement

No potential conflict of interest was reported by the authors.

References

Bazilevs, Y., Calo, V. M., Cottrell, J. A., Evans, J. A., Hughes, T. J. R., Lipton, S., ... Sederberg, T. W. (2010). Isogeometric analysis using T-Splines. *Computer Methods in Applied Mechanics and Engineering, 199*, 229–263.

Benson, D. J., Bazilevs, Y., Hsu, M. C., & Hughes, T. J. R. (2010). Isogeometric shell analysis: The Reissner–Mindlin shell. *Computer Methods in Applied Mechanics and Engineering, 199*, 276–289.

Cardoso, R. P. R. (2002). *Development of one point quadrature shell elements with anisotropic material models for sheet metal forming analysis* (PhD thesis), University of Aveiro, Portugal.

Cardoso, R. P. R., & Yoon, J. W. (2005). One point quadrature shell elements for sheet metal forming analysis. *Archives of Computational Methods in Engineering, 12*, 3–66.

Cardoso, R. P. R., & Yoon, J. W. (2007). One point quadrature shell elements: A study on convergence and patch tests. *Computational Mechanics, 40*, 871–883.

Cardoso, R. P. R., & Cesar de Sa, J. M. A. (2012). The enhanced assumed strain method for the isogeometric analysis of nearly incompressible deformation of solids. *International Journal for Numerical Methods in Engineering, 92*, 56–78.

Cardoso, R. P. R., & Cesar de Sa, J. M. A. (2014). Blending moving least squares techniques with NURBS basis functions for nonlinear isogeometric analysis. *Computational Mechanics, 53*, 1327–1340.

Cesar de Sa, J. M. A., & Owen, D. R. J. (1986). The imposition of the incompressible constraints in finite elements – A review of approaches with a new insight to the locking phenomenon. In *Numerical methods for non-linear problems*. Pineridge Press.

Cesar de Sa, J. M. A., & Natal Jorge, R. M. (1999). New enhanced strain elements for incompressible problems. *International Journal for Numerical Methods in Engineering, 44*, 229–248.

Cottrell, J. A., Reali, A., Bazilevs, Y., & Hughes, T. J. R. (2006). Isogeometric analysis of structural vibrations. *Computer Methods in Applied Mechanics and Engineering, 195*, 5257–5296.

Cottrell, J. A., Hughes, T. J. R., & Reali, A. (2007). Studies of refinement and continuity in isogeometric structural analysis. *Computer Methods in Applied Mechanics and Engineering, 196*, 4160–4183.

Cottrell, J. A., Hughes, T. J. R., & Bazilevs, Y. (2009). *Isogeometric analysis, toward integration of CAD and FEA*. Wiley.

Deseri, L., & Owen, D. R. (2002). Invertible structured deformations and the geometry of multiple slip in single crystals. *International Journal of Plasticity, 18*, 833–849.

Deseri, L., & Owen, D. R. (2016). Submacroscopic disarrangements induce a unique, additive and universal decomposition of continuum fluxes. *Journal of Elasticity, 122*, 223–230.

Echter, R., & Bischoff, M. (2010). Numerical efficiency, locking and unlocking of NURBS finite elements. *Computer Methods in Applied Mechanics and Engineering, 199*, 374–382.

Hughes, T. J. R., Cohen, M., & Haroun, M. (1978). Reduced and selective integration techniques in finite element analysis of plates. *Nuclear Engineering Design, 46*, 203–22.

Hughes, T. J. R. (2000). *The finite element method: Linear static and dynamic finite element analysis* (2nd ed.). Englewood Cliffs, NJ: Prentice-Hall.

Hughes, T. J. R., Cottrel, J. A., & Bazilevs, Y. (2005). Isogeometric analysis: CAD, finite elements, NURBS, exact geometry and mesh refinement. *Computer Methods in Applied Mechanics and Engineering, 194*, 4135–4195.

Hughes, T. J. R., Reali, A., & Sangalli, G. (2008). Duality and unified analysis of discrete approximations in structural dynamics and wave propagation: Comparison of p-method

finite elements with k-method NURBS. *Computer Methods in Applied Mechanics and Engineering*, *197*, 4104–4124.

Hughes, T. J. R., Reali, A., & Sangalli, G. (2010). Efficient quadrature for NURBS-based isogeometric analysis. *Computer Methods in Applied Mechanics and Engineering*, *199*, 301–313.

Laursen, T. A., & Simo, J. C. (1993). Algorithmic symmetrization of Coulomb frictional problems using augmented Lagrangians. *Computer Methods in Applied Mechanics and Engineering*, *108*, 133–146.

Laursen, T. A. (2002). *Computational contact and impact mechanics: Fundamentals of modeling interfacial phenomena in nonlinear finite element analysis*. Berlin: Springer-Verlag.

Oldenburg, M., & Nilsson, L. (1994). The position code algorithm for contact searching. *International Journal for Numerical Methods in Engineering*, *37*, 359–386.

Ortiz, M., & Simo, J. C. (1986). An analysis of a new class of integration algorithms for elastoplastic relations. *International Journal for Numerical Methods in Engineering*, *23*, 353–366.

Piegl, L., & Tiller, W. (1996). *The NURBS Book*. Berlin: Springer-Verlag.

Simo, J. C., & Hughes, T. J. R. (1998). *Computational inelasticity. Interdisciplinary applied mathematics* (Vol. 7). New York, NY: Springer.

Taylor, R. L. (2010). Isogeometric analysis of nearly incompressible solids. *International Journal for Numerical Methods in Engineering*, *87*, 273–288.

Yoon, J. W., Yang, D. Y., & Chung, K. (1999). Elasto-plastic finite element method based on incremental deformation theory and continuum based shell elements for planar anisotropic sheet materials. *Computer Methods in Applied Mechanics and Engineering*, *174*, 23–56.

Wriggers, P. (2002). *Computational contact mechanics*. Berlin: Springer-Verlag.

Appendix 1. Derivatives of NURBS basis functions

The derivatives of $R_{IJK}(\xi,\eta,\zeta)$ in order to the NURBS parametric coordinates are obtained from:

$$\begin{aligned}
\frac{\partial R_{IJK}(\xi,\eta,\zeta)}{\partial \xi} &= \frac{N_K^r(\zeta)\,N_I^q(\eta)\,N_{J,\xi}^p(\xi)\,W_{IJK}}{W} - \frac{N_J^p(\xi)\,N_I^q(\eta)\,N_K^r(\zeta)\,W_{IJK}}{W^2}W_{,\xi} \\
\frac{\partial R_{IJK}(\xi,\eta,\zeta)}{\partial \eta} &= \frac{N_K^r(\zeta)\,N_{I,\eta}^q(\eta)\,N_J^p(\xi)\,W_{IJK}}{W} - \frac{N_J^p(\xi)\,N_I^q(\eta)\,N_K^r(\zeta)\,W_{IJK}}{W^2}W_{,\eta} \\
\frac{\partial R_{IJK}(\xi,\eta,\zeta)}{\partial \zeta} &= \frac{N_{K,\zeta}^r(\zeta)\,N_I^q(\eta)\,N_J^p(\xi)\,W_{IJK}}{W} - \frac{N_J^p(\xi)\,N_I^q(\eta)\,N_K^r(\zeta)\,W_{IJK}}{W^2}W_{,\zeta}
\end{aligned} \tag{A1}$$

where the derivatives of W can be easily obtained from the derivatives of the basis functions in Equation (9) for 2D patches or Equation (10) for 3D patches:

$$\begin{aligned}
W_{,\xi} &= \sum_{I=1}^{n}\sum_{J=1}^{m} N_I^q(\eta)\,\frac{dN_J^p(\xi)}{d\xi}W_{IJ} \\
W_{,\eta} &= \sum_{I=1}^{n}\sum_{J=1}^{m} \frac{dN_I^q(\eta)}{d\eta}N_J^p(\xi)\,W_{IJ}
\end{aligned} \tag{A2}$$

for the 2D NURBS and:

$$
\begin{aligned}
W_{,\xi} &= \sum_{k=1}^{l}\sum_{I=1}^{n}\sum_{J=1}^{m} N_K^r(\zeta)\, N_I^q(\eta)\, \frac{dN_J^p(\xi)}{d\xi}\, W_{IJK} \\
W_{,\eta} &= \sum_{k=1}^{l}\sum_{I=1}^{n}\sum_{J=1}^{m} N_K^r(\zeta)\, \frac{dN_I^q(\eta)}{d\eta}\, N_J^p(\xi)\, W_{IJK} \\
W_{,\zeta} &= \sum_{k=1}^{l}\sum_{I=1}^{n}\sum_{J=1}^{m} \frac{dN_K^r(\zeta)}{d\zeta}\, N_I^q(\eta)\, N_J^p(\xi)\, W_{IJK}
\end{aligned}
\tag{A3}
$$

for the 3D NURBS.

Appendix 2. Control points and knot vectors for the rigid die tool

In Table B1, the distribution of the control points along the longitudinal direction of the lower die tool for the coarser 'mesh' example (for $z = .0$) is presented. The depth of the lower die tool is generated by extruding the control points from Table B1 along the z-direction.

Table B1. Control points for the lower die tool.

	Coordinates and weight factor			
CP number	x	y	z	w
1	−100.000000	−.500000	.000000	1.000000
2	−25.000000	−.500000	.000000	1.000000
3	125.000000	−.500000	.000000	1.000000
4	200.000000	−.500000	.000000	1.000000
5	220.710678	−.500000	.000000	.853553
6	250.000000	−29.789322	.000000	.853553
7	250.000000	−50.500000	.000000	1.000000
8	250.000000	−63.000000	.000000	1.000000
9	250.000000	−88.000000	.000000	1.000000
10	250.000000	−100.500000	.000000	1.000000
11	250.000000	−121.210678	.000000	.853553
12	279.289322	−150.500000	.000000	.853553
13	300.000000	−150.500000	.000000	1.000000
14	320.710678	−150.500000	.000000	.853553
15	350.000000	−121.210678	.000000	.853553
16	350.000000	−100.500000	.000000	1.000000
17	350.000000	−79.789322	.000000	.853553
18	379.289322	−50.500000	.000000	.853553
19	400.000000	−50.500000	.000000	1.000000
20	475.000000	−50.500000	.000000	1.000000
21	625.000000	−50.500000	.000000	1.000000
22	700.000000	−50.500000	.000000	1.000000

In Table B2, the distribution of the control points for the upper die also along the longitudinal direction ($z = .0$) and after the offset from the lower die tool is given.

Table B2. Control points for the upper die tool.

CP number	Coordinates and weight factor			
	x	y	z	w
265	−100.000000	154.500000	.000000	1.000000
266	−25.000000	154.500000	.000000	1.000000
267	125.000000	154.500000	.000000	1.000000
268	200.000000	154.500000	.000000	1.000000
269	222.624103	154.119394	.000000	.853553
270	254.614735	122.135314	.000000	.853553
271	255.000000	99.500000	.000000	1.000000
272	255.000000	87.000000	.000000	1.000000
273	255.000000	62.000000	.000000	1.000000
274	255.000000	49.500000	.000000	1.000000
275	254.614735	30.713958	.000000	.853553
276	281.213958	4.114735	.000000	.853553
277	300.000000	4.500000	.000000	1.000000
278	318.786042	4.114735	.000000	.853553
279	345.385265	30.713958	.000000	.853553
280	345.000000	49.500000	.000000	1.000000
281	345.385265	72.135314	.000000	.853553
282	377.364686	104.114735	.000000	.853553
283	400.000000	104.500000	.000000	1.000000
284	475.000000	104.500000	.000000	1.000000
285	625.000000	104.500000	.000000	1.000000
286	700.000000	104.500000	.000000	1.000000

Table B3 shows the knot vector along ξ-direction that was used for both dies (for the coarser 'mesh' example). A degree 2 was used for the NURBS basis functions.

Table B3. Knot vector used for both dies.

Knot number	ξ
1	.000000
2	.000000
3	.000000
4	.500000
5	1.000000
6	1.000000
7	1.500000
8	2.000000
9	2.000000
10	2.500000
11	3.000000
12	3.000000
13	3.500000
14	4.000000
15	4.000000
16	4.500000
17	5.000000
18	5.000000
19	5.500000
20	6.000000
21	6.000000
22	6.500000
23	7.000000
24	7.000000
25	7.000000